

Catalysis Science & Technology

Accepted Manuscript

This article can be cited before page numbers have been issued, to do this please use: A. Shafiq, I. Danylo, L. Kolacny, B. Sevez, J. Luxa, M. Vesely and M. Pitinova, *Catal. Sci. Technol.*, 2026, DOI: 10.1039/D5CY01520K.



This is an Accepted Manuscript, which has been through the Royal Society of Chemistry peer review process and has been accepted for publication.

Accepted Manuscripts are published online shortly after acceptance, before technical editing, formatting and proof reading. Using this free service, authors can make their results available to the community, in citable form, before we publish the edited article. We will replace this Accepted Manuscript with the edited and formatted Advance Article as soon as it is available.

You can find more information about Accepted Manuscripts in the [Information for Authors](#).

Please note that technical editing may introduce minor changes to the text and/or graphics, which may alter content. The journal's standard [Terms & Conditions](#) and the [Ethical guidelines](#) still apply. In no event shall the Royal Society of Chemistry be held responsible for any errors or omissions in this Accepted Manuscript or any consequences arising from the use of any information it contains.

HYDROGENATION OF CINNAMALDEHYDE BY PLATINUM SUPPORTED ON 2D AND 3D TRANSITION METAL SULFIDES

Ayesha Shafiq^a, Iryna Danylo^a, Lukas Kolacny^a, Berke Sevemez^a, Jan Luxa^b, Martin Vesely^a, Martina Pitinova^{a*}

The selective hydrogenation of cinnamaldehyde (CAL), a model α , β -unsaturated aldehyde, yields valuable products such as cinnamyl alcohol (COL) and hydrocinnamaldehyde (HCAL). Pt-based catalysts supported on transition metal dichalcogenides (MoS_2 , WS_2 , and their composite) in bulk forms and their exfoliated counterparts were synthesized using microwave-assisted and wet impregnation methods. Characterization (SEM/EDS, TEM, XRF, XRD, BET) confirmed ~ 9 wt.% Pt loading, preserved layered structures, and well-dispersed nanoparticles. Catalyst based on 2D supports provided finer Pt dispersion (2–6 nm), with microwave synthesis yielding smaller, more uniform particles, especially in Mo-W composite. Catalytic testing demonstrated that both activity and selectivity were strongly influenced by the support composition and morphology, with 2D Mo-W composite outperforming MoS_2 and WS_2 . All catalysts predominantly promoted selective C=O hydrogenation to COL, while HCAL, and HCAL remained minor products. The best performance was achieved with Pt supported on 2D Mo-W-S composite prepared by microwave-assisted synthesis, delivering 75% CAL conversion with COL selectivity and yield achieved within 6 h, 64% and 48%, respectively.

Received 00th January 20xx,
Accepted 00th January 20xx

DOI: 10.1039/x0xx00000x

Introduction

The selective hydrogenation of α , β -unsaturated aldehydes is a key route to unsaturated alcohols used in pharmaceuticals, fragrances, and food additives. Cinnamaldehyde (CAL), a model compound with an aromatic ring, C=C, and C=O groups, produces three main hydrogenation products, with cinnamyl alcohol (COL) being the most valuable intermediate. Its transformation is surface-catalyzed and strongly influenced by catalyst properties, reaction conditions, and adsorption behavior. Cinnamaldehyde (CAL) hydrogenation proceeds via two main pathways, selective C=O hydrogenation forming cinnamyl alcohol (COL) or C=C hydrogenation yielding hydrocinnamaldehyde (HCAL)¹. Both of these groups further hydrogenate to form final product hydrocinnamyl alcohol (HCOL) as shown in reaction scheme **Figure 1**. The HCAL pathway is thermodynamically more favorable because of lower bond energy of alkene group (615 kJ/mol) compared to carbonyl group (715 kJ/mol) and the π^4 adsorption mode².

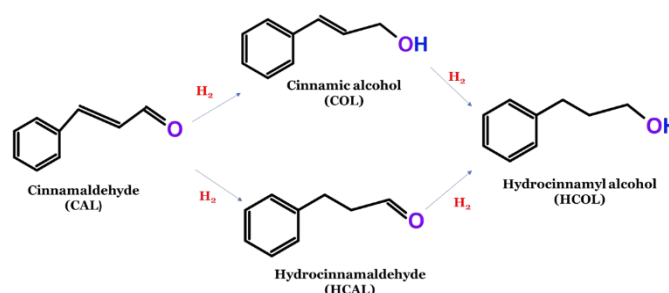


Figure 1: Scheme of cinnamaldehyde hydrogenation (CAL) to cinnamyl alcohol (COL), hydrocinnamaldehyde (HCAL), and hydrocinnamyl alcohol (HCOL).

While HCAL serves as an intermediate in pharmaceutical synthesis, particularly for HIV treatments³, COL is the preferred product because of its broad applications in pharmaceuticals, fragrances, fine chemicals, and the food industry^{4,5}. Therefore, although thermodynamics favors (C=C) hydrogenation toward HCAL, achieving high selectivity toward COL requires precise control of catalyst surface properties and adsorption modes. Consequently, significant research efforts have been directed toward designing catalysts that selectively hydrogenate the carbonyl (C=O) group while preserving the carbon-carbon double bond (C=C). Product distribution in cinnamaldehyde (CAL) hydrogenation depends on catalyst type, solvent, additives, and reaction conditions. Selectivity is closely related to the d-bandwidth of the metal catalyst, as greater orbital

^a Department of Organic Technology, University of Chemistry and Technology, 166 28 Prague, Czech Republic.

^b Department of Inorganic Chemistry, University of Chemistry and Technology, 166 28 Prague, Czech Republic



extension enhances cinnamyl alcohol (COL) formation. Metals with large d-bandwidths such as Pt, Ru, and Ir are therefore commonly employed. Over recent decades, both homogeneous and heterogeneous catalytic systems have been explored to address this selectivity challenge.⁶ Homogeneous catalysts offer high selectivity through ligand-controlled steric and electronic effects but face limitations such as difficult separation, low reusability, and possible contamination, which restrict practical applications⁷. To overcome these issues, extensive research has focused on developing heterogeneous catalysts using both noble and non-noble metals. Literature reports highlight the use of noble metal-based catalysts, including Pt, Pd, Au, and Ru, for efficient cinnamaldehyde (CAL) hydrogenation^{8–11}. Non-noble metal catalysts such as Co, Cu, and Ni have also been explored for CAL hydrogenation^{12–15}. Yuan et al.¹⁶ reported that bimetallic CoPt nanoparticles supported on Fe₃O₄ achieved 95% CAL conversion with 84% selectivity to COL. In contrast, Cu-based catalysts showed poor conversion and selectivity¹⁷. Ni-based systems generally favored HCAL formation, as Mohire et al.¹⁸ achieved 100% HCAL selectivity at 89% CAL conversion using a Ni-Cu-RGO catalyst. Similarly, Pd-based catalysts tend to promote C=C bond hydrogenation, leading to higher HCAL yields, for instance, Chen et al.¹⁹ developed Pd nanoparticles encapsulated in a mesoporous carbon matrix, producing HCAL as the main product with 80% selectivity. Product selectivity in CAL hydrogenation is influenced not only by the choice of metal but also by the solvent, support, and catalyst morphology. The preparation method and nanoparticle distribution play a critical role as well^{20,21}. The location of Ru nanoparticles on carbon nanotubes (CNTs) strongly affected CAL hydrogenation selectivity, Ru encapsulated within CNT channels favored C=O hydrogenation due to confinement effects, while Ru deposited on the outer CNT walls promoted preferential C=C hydrogenation²². Gold (Au) and iridium (Ir) based catalysts have also been investigated for CAL hydrogenation. In the case of Au, COL selectivity varied widely (10-90%) when uniform nanoparticles were supported on different oxides such as MgO, Al₂O₃, TiO₂, Fe₂O₃, Co₃O₄, ZnO, and In₂O₃, strongly influenced by the acidic or basic nature of the oxide supports²³.

Among the noble metals investigated, platinum-based catalysts have emerged as particularly promising systems due to their tuneable electronic structure and strong metal-support interactions. Platinum-based (Pt) catalysts are highly effective in the selective hydrogenation of cinnamaldehyde (CAL), generally favoring cinnamyl alcohol (COL) as the main product. However, their high activity can also cause over-hydrogenation to hydrocinnamyl alcohol (HCOL), since Pt promotes both C=O and, to some extent, C=C bond hydrogenation. To enhance COL selectivity and suppress over-hydrogenation, a range of Pt-based monometallic and bimetallic catalysts have been developed^{24–28}, achieving over 90% CAL conversion with more than 90% COL selectivity. These improvements rely on strategies such as optimizing support materials, controlling Pt size and dispersion, adjusting reaction conditions, and tailoring

metal support interactions to guide the reaction pathway. Product selectivity, however, can still vary within the same catalytic system depending on reaction conditions and support morphology. Wei et al.²⁹ demonstrated structure-dependent selectivity in Pt/CeO₂-ZrO₂ catalysts, where changes in the Ce:Zr molar ratio significantly influenced COL selectivity, highlighting the key role of Pt-support interactions. Despite these advances, achieving consistent and controllable selectivity toward COL remains challenging, as product distribution strongly depends on metal dispersion, electronic properties, and support effects. In this context, exploring novel support materials capable of modulating Pt electronic structure and adsorption behaviour represents a promising strategy.

Although significant progress has been achieved with oxide, carbon, and metal-supported catalysts, several challenges remain, particularly regarding the role of the support in governing adsorption behaviour and reaction selectivity. In a recent study Wang et al. systematically investigated a series of Pt catalysts supported on different metal oxides (Pt/MO_x) for the selective hydrogenation of cinnamaldehyde (CAL). Their results clearly demonstrated that the nature of the support plays a decisive role in determining both catalytic activity and product selectivity. Specifically, Mn₂O₃ and Fe₂O₃ were identified as favourable supports for preferential adsorption of the C=O functional group, thereby promoting selective hydrogenation toward the unsaturated alcohol. In contrast, TiO₂ exhibited a stronger interaction with the C=C bond, as evidenced by FTIR analysis, leading to a shift in selectivity toward C=C hydrogenation products.³⁰ These findings highlight the critical influence of support properties on substrate adsorption modes and, consequently, on chemo selectivity in CAL hydrogenation. In another study, Patil et al. in their review briefly discussed catalyst design strategies for selective CAL hydrogenation, highlighting the influence of metal type, preparation method, and structural properties on chemo selectivity toward COL or HCAL.³¹

In this context, exploring alternative support materials that can modulate metal-support interactions in a more controlled and effective manner becomes highly relevant. Two-dimensional (2D) transition metal dichalcogenides (TMDs) have gained considerable interest for their unique chemical, electronic, mechanical, and magnetic properties. Their multifunctionality makes them promising for applications in spintronics, optoelectronics, sensing, catalysis, and energy-related technologies.^{32,33} MoS₂ has been widely explored as a support for various metals such as Fe, Co, Ni, Cu, Ru, Rh, Pd, and Ag in CO₂ hydrogenation.³⁴ Pt has also been effectively integrated with MoS₂, for instance, Pt monomers anchored on MoS₂ nanosheets achieved a high loading of 7.5% while maintaining atomic dispersion, where synergistic interactions between adjacent Pt monomers greatly enhanced CO₂ hydrogenation performance.³⁵ Similarly, Xu et al.³⁶ deposited Pt on MoS₂ via wet impregnation method to study hydrogen evolution reaction (HER) kinetics and reported superior performance of the Pt-



MoS₂ system compared to Pt/C. Although transition metal dichalcogenide (TMD)-supported metals have demonstrated remarkable performance in hydrogenation reactions such as CO₂ conversion and HER, their potential in hydrogenation of α , β -unsaturated aldehydes remain largely unexplored. Various synthesis techniques have been employed to tune Pt nanoparticle size and density, including electron beam lithography for fabricating Pt-based 2D materials.³⁷ Many reported systems involve complex synthesis procedures.³⁸ In this study, we systematically investigate Pt–TMD catalysts synthesized by simple preparation methods including via microwave-assisted and wet impregnation methods, supported on MoS₂, WS₂, and Mo–W–S composites in both bulk (3D) and nanosheet (2D) forms. By directly comparing morphology, composition, and synthesis route, this work establishes structure–selectivity relationships and demonstrates the advantages of TMD supports over traditional systems in controlling catalytic activity and product distribution.

Experimental

Materials

Cinnamaldehyde (*trans*-cinnamaldehyde, 97 %), chloroplatinic acid hexahydrate (H₂PtCl₆·6H₂O) were supplied by Merck KGaA (Darmstadt, Germany), ethylene glycol (G. R.) and isopropyl alcohol (G. R., iso reagent) was supplied by Lach-Ner, s.r.o. (Neratovice, Czech Republic) and mesitylene (purity., > 99.0 %) by Fluka (Buchs, Switzerland). Granulated sulphur (99.999 %), molybdenum powder (99.95 %, -100mesh), tungsten powder (99.9 %, -100 mesh), were obtained from Strem, USA. 5% Pt/Alumina was obtained from Johnson Matthey (123 powder, Royston, United Kingdom).

Synthesis of Layered Transition Metal Dichalcogenides

Molybdenum disulfide (MoS₂), tungsten disulfide (WS₂) and their composite (Mo_{0.25}W_{0.75}S₂) were synthesized by reacting powdered metals with elemental chalcogens in vacuum sealed quartz ampoules, followed by controlled thermal treatments reported by Sofer et al.³⁹ Transition metals and chalcogens were weighed in stoichiometric ratios (± 1 mg) to prepare 10 g of transition metal dichalcogenide (TMD), with an additional 30 mg of chalcogen added to ensure excess. The mixture was sealed in an evacuated ampoule (pressure < 5 × 10⁵ mbar) and preheated with a 300 °C heat gun for 2 minutes. Ampoules were then melt-sealed using an oxygen-hydrogen torch. The sealed ampoules were heated at 425 °C for 24 hours in a muffle furnace, followed by a gradual temperature increase to 500 °C over 24 hours and subsequent cooling. After 10 minutes of mechanical homogenization, samples were heated at 600 °C for 48 hours (heating/cooling rate: 5 °C/0.0167h). A second homogenization was followed by heating at 800 °C for 48 hours, then 850 °C for 12 hours under the same rate conditions. For MoS₂, the final step was modified to 700 °C for 72 hours to prevent 3R phase formation. Excess chalcogen was removed by heating one end of the ampoule to 600 °C for 30 minutes while keeping the other end at room temperature.

Catalyst preparation

Catalysts were synthesized using bulk TMDs (MoS₂, WS₂ and Mo–W–S) and their 2D counterparts via two distinct methods, simple wet impregnation and microwave-assisted impregnation, both with in-situ chemical reduction⁴⁰. In both approaches, an impregnation mixture was prepared by mixing 272.7 mL of ethylene glycol (reducing agent), 27.2 mL of deionized water (solvent), 1.56 mL of 0.04 M H₂PtCl₆·6H₂O solution (Pt precursor), and 120 mg of support material (MoS₂, WS₂ or Mo–W–S). A nominal Pt loading of 9.2 wt.% was applied to all catalysts. A deliberately high Pt content was selected to clearly isolate and quantify the promotional effect of Pt on catalytic performance, ensuring that any observed activity trends could be attributed unambiguously to Pt rather than to support-related limitations.

Wet impregnation with chemical reduction. The impregnation mixture was first subjected to ultrasonic treatment for 4 hours to ensure additional exfoliation of 2D nanosheets (in case of 2D analogues of TMDs) and uniform dispersion of Pt NPs over the support. It was then transferred to an oil bath and stirred under reflux (120 °C, oil bath) for 20 hours. After cooling, the resulting catalyst was filtered, washed with deionized water, and dried in a vacuum oven at 60 °C for 24 hours. Activation of the prepared catalysts was carried out by reduction in the calcination oven under the stream of a hydrogen and nitrogen (H₂/N₂ = 40/60 (v/v)) at 250 °C for 2 h (temperature ramp of 250 °C/360 min) prior testing in hydrogenation reaction.

Microwave-Assisted wet Impregnation with chemical reduction. The prepared impregnation mixture was placed in a microwave oven (UWave-2000 Multifunctional Microwave Chemistry Reaction Workstation, Sineo) and irradiated for 4 minutes (500 W), followed by a 4-minute rest period. The temperature was maintained at 80 °C for 12 minutes, increasing slightly to 86 °C due to continuous sonication. The mixture was also subjected to ultrasonic treatment for 21 minutes and 40 seconds to enhance exfoliation (in case of 2D nanosheets) and enhance Pt dispersion. After this impregnation process, the catalyst was treated as in case of simple wet impregnation, filtration, washing, drying and reduction (the stream of a hydrogen and nitrogen gas stream H₂/N₂ = 40/60 (v/v) at 250 °C for 2 h). For better understanding, Table 1 provides description about used support for catalyst preparation, preparation method and catalyst labelling.

Cinnamaldehyde hydrogenation

For hydrogenation, high pressure autoclave Parr (volume 100 mL) was used in batch mode. 2.7g of cinnamaldehyde (reactant) was mixed with 50 mL of isopropyl alcohol (solvent), and 400 μ L of mesitylene (internal standard for GC analysis). A zero sample was taken before starting the reaction. Subsequently, 27 mg of catalyst was then added to the reaction mixture and sealed in the autoclave. Before pressurizing the system, autoclave was flushed three times with nitrogen and once with hydrogen. The reaction was performed under 1 MPa hydrogen pressure, at a temperature of 80 °C and stirred at 800 rpm.

View Article Online

DOI: 10.1039/D5CY01520K



Table 1: Pt-based catalyst prepared using various supports and their preparation methods

Support	Support	Preparation method	Catalyst label
MoS ₂	2D	WIR	Pt/2D-MoS ₂ -WIR
		MW	Pt/2D-MoS ₂ -MW
	3D	WIR	Pt/3D-MoS ₂ -WIR
		MW	Pt/3D-MoS ₂ -MW
WS ₂	2D	WIR	Pt/2D-WS ₂ -WIR
		MW	Pt/2D-WS ₂ -MW
	3D	WIR	Pt/3D-WS ₂ -WIR
		MW	Pt/3D-WS ₂ -MW
Mo-W-S	2D	WIR	Pt/2D-Mo-W-S-WIR
		MW	Pt/2D-Mo-W-S-MW
	3D	WIR	Pt/3D-Mo-W-S-WIR
		MW	Pt/3D-Mo-W-S-MW

Note: 3D = bulk, 2D = nano, WIR = wet impregnation with chemical reduction, MW= microwave-assisted impregnation with chemical reduction

The progress of the reaction was observed by analyzing samples at set intervals times (30, 60, 120, 240 and 360 minutes) taken via capillary sampling. The reaction was performed for a maximum of 360 minutes. Before subjecting to GC, samples were centrifuged at 8000 rpm for 5 minutes, and supernatant was further filtered and analyzed using GC (SHIMADZU GC 2014 with FID detector a capillary column SPB5 with length 30 m, width 0.32 mm a stationary phase 0.25 μm).

The evaluated catalysts were assessed based on their activity, measured by conversion after 360 minutes and the achieved selectivities toward hydrogenation products.

Conversion of cinnamaldehyde (%)

$$X_t = \frac{C_{CAL,0} - C_{CAL,t}}{C_{CAL,0}} * 100\% \quad (1)$$

Selectivity toward products (%)

$$S_t = \frac{n_{t,t}}{\sum n_{products,t}} * 100\% \quad (2)$$

Reaction rates (mmol·min⁻¹·mg_{Pt}⁻¹)

$$r_0 = \frac{C_{CAL,0} - C_{CAL,t1}}{t_1 * m_{gPt}} * L \quad (3)$$

$$r_t = \frac{C_{CAL,t2} - C_{CAL,t3}}{(t_3 - t_2) * m_{gPt}} * L \quad (4)$$

Turn over frequency was calculated using equations given below

Moles of CAL converted

$$r_{avg} = \frac{(n_{CAL,0} - n_{CAL,t}) * V}{t} \quad (5)$$

Moles of Pt

$$n_{Pt} = \frac{m_{cat} * \omega_M}{MW_m} \quad (6)$$

Pt dispersion from TEM

$$D = (3.32 * \frac{d_{Pt}}{d_p})^{0.813} \quad (7)$$

$$n_{Pt, surface} = D * n_{Pt} \quad (8)$$

Turn over frequency

$$\frac{r_{avg}}{n_{Pt, surface}} \quad (9)$$

View Article Online
DOI: 10.1039/D5CY01520K

In the equations $C_{CAL,0}$ and $C_{CAL,t}$ are initial and actual concentration of cinnamaldehyde (mmol/L), $c_{i,t}$ is actual concentration of selected product (mmol/L), $n_{i,t}$ is actual number of moles of selected product (mmol), t is reaction time (min), t_1 is reaction time for calculating of initial reaction rate (30 min in this case, which is time of taking the first sample), r_0 is initial reaction rate (mmol/(min·mg_{Pt})), and r_t is reaction rate at higher reaction times (mmol/(min·mg_{Pt})). Rate of reactions were calculated with and without considering catalyst mass and metal loadings. Turn over frequency was calculated using number of moles of cinnamaldehyde converted at 360 minute and surface dispersion of platinum nanoparticles using average diameter obtained from TEM analysis. (eq 5- 9). In equation 5, $n_{CAL,t}$ is molar concentration of cinnamaldehyde at 360 minute. In equation m_{cat} is amount of catalyst used in reaction (g), ω_M is metal loading in catalyst (from XRF), MW_m is molecular mass of platinum. Platinum dispersion on surface was calculated using equation 7⁴¹, where d_{Pt} is platinum atomic diameter 0.277 nm, and d_p is average size of nanoparticles obtained from TEM.

Catalyst characterization

All catalysts were characterized in their final active form- after the reduction at 250 °C in hydrogen atmosphere.

Scanning electron microscopy (SEM) and energy dispersive spectroscopy (EDS) were used for identification of surface morphology and elemental composition of the catalysts. SEM images were obtained using a TESCAN LYRA3 GMU dual-beam scanning electron microscope (TESCAN, Brno, Czech Republic) equipped with a field emission gun (FEG). Elemental analysis and radial profile measurements were performed with an energy-dispersive X-ray spectrometer (EDS) featuring an 80 mm² SDD detector (X-MaxN, Oxford Instruments, Abingdon, Oxfordshire, England), processed using AZtecEnergy software. Quantitative element analysis of the prepared and reduced catalysts was performed using fully automatic sequential X-ray fluorescence spectrometer (XRF) Axios (PANalytical, Holland). XRF spectrometer was equipped with Rh tube, 4kW generator, 3 collimators, 8 crystals (PX1, PX4a, PX5, PX7, PE002, Ge 111, LiF 200, LiF 220) and 2 detectors- proportional and scintillation. Standardless analysis was done with program Omnian. After synthesizing the catalyst, the reaction mixture was filtered to separate the solid catalyst. The collected filtrate was subsequently analysed by an Agilent 5900 ICP-OES (inductively coupled plasma optical emission spectrometer) to determine the extent of platinum (Pt) loss during the filtration process. The plasma was formed in a flow of Ar gas by externally applied radio frequency field of 1.2 kW. The measurement was conducted in synchronous vertical dual view (SVDV) mode, allowing both the axial and radial views of the plasma to be captured in one reading, allowing fast but very accurate analysis. The quantitative analysis was allowed by the use of 5-point calibration curve for each element measured. The measurement used an inner standard of yttrium at the



wavelength of 371.029 nm. Each sample was measured in 3 duplicates with 5s reading time each. Spectral intensities for Pt were measured at the wavelength of 214.424. The measured values were obtained using the ICP Expert Pro Software. Following filtration, the catalyst retained on the filter paper was washed three times with distilled water to ensure the removal of any residual soluble species. The combined washing solutions were subsequently subjected to analysis by atomic absorption spectrometry (AAS) in order to evaluate whether any platinum loss had occurred during the washing step. The measurements were performed using an Agilent 280FS AA spectrometer equipped with flame atomization. For platinum determination, an acetylene–air flame was applied at a wavelength of 265.9 nm.

Transmission electron microscope was used for particle size measurement. Images were acquired at EFTEM with specification Jeol 2200 FS (JEOL, Tokyo, Japan). The crystallinity of the prepared catalysts was analyzed using the X-ray diffraction (XRD) method. Measurements were conducted at room temperature with a Bruker-Phaser 2nd Generation powder diffractometer, utilizing CuK α radiation (λ [CuK- α 1] = 1.54056×10^{-1} nm, λ [CuK- α 2] = 1.54443×10^{-1} nm). Data acquisition was performed using a high-speed 1D PIXCEL detector over a 2θ range of 4.99–90.019°, with a time step of 0.5 s, resulting in a total scan time of 886.4 s. The collected data were analyzed using HighScore Plus software. The specific surface areas of the prepared and reduced catalysts were determined via nitrogen adsorption–desorption measurement using NOVA 2000e surface area and pore size analyzer (Quantachrome Instruments, Anton Paar GmbH – Headquarters, Graz, Austria). Helium was used for the calibration of the measuring cells. The samples were outgassed at 150 °C for 3 h before each measurement. The BET equation was used for calculating the specific surface area of the catalysts.

XPS measurements were performed with an ESCA Probe P (electron spectroscopy for chemical analysis) instrument (from Omicron Nanotechnology Ltd., 2005) with a monochromatic Al-K α X-ray source (1486.6 eV), operating at 15 kV, 105W and with a hemispheric analyzer. The operating vacuum was kept at $\sim 5 \times 10^{-10}$ mbar inside the analysis chamber. Calibration was performed using binding energies of Cu2p $_{3/2}$ (932.7 eV) and Ag3d $_{5/2}$ (368.26 eV), with full width at half maximum (FWHM) values for Cu2p $_{3/2}$ (0.85 eV) and Ag3d $_{5/2}$ (0.67 eV). For all samples were recorded survey and high-resolution scans C1s, O1s, Pt4f, Mo3d, W4f and S2p. A compromise between resolution and acquisition time is obtained when a pass energies 50 eV resp. 30 eV, step 0.4 resp. 0.1 eV was used for survey resp. high resolution scans. The surface charges during the XPS spectra acquisition were corrected by applying a very small current on the surface by a flood gun emission system. Etching of the surface film was conducted using XPS to obtain information about the nature of oxide film. The spectra were evaluated using CasaXPS software 2.3.13Dev10, employing

Shirley background subtraction and Gaussian-Lorentzian functions (GL(30)). An adventitious carbon C1s peak at 285.13 eV was used for calibration of the spectra (to correct the position).

Results and discussion

Current study focuses on the use of MoS $_2$, WS $_2$ and their composite Mo-W-S in their bulk and 2D exfoliated forms, as a support material for the preparation of Pt based catalyst. Furthermore, this work focuses on evaluation of these catalytic supports in CAL hydrogenation. As mentioned in the introduction, the preparation method can influence the physicochemical properties of the resulting catalysts and, consequently, affect catalytic activity. Therefore, two preparation methods were employed for catalyst synthesis: simple wet impregnation and a microwave-assisted technique, both conducted in the presence of ethylene glycol as a reducing agent.

X-ray Fluorescence (XRF)

To evaluate the efficiency of different preparation techniques and to determine the elemental composition of the samples, with particular emphasis on the actual platinum loading, X-ray fluorescence (XRF) analysis was employed. The results obtained from XRF are summarized in **Table 2**. The nominal Pt loading was fixed at 9.2 wt% for all prepared catalysts. For MoS $_2$ -based catalysts, the actual Pt loading closely matched the targeted value. MoS $_2$ -supported catalysts exhibited higher Pt loadings than the other supports within the study, regardless of the synthesis method. In contrast, for WS $_2$, the wet impregnation reduction (WIR) method yielded a Pt content of 9.0 wt%, which is in good agreement with the nominal loading, whereas the microwave-assisted (MW) method proved unsuitable for this support. Only low Pt contents were obtained for the bulk and 2D WS $_2$ analogues, namely 1.2 wt% and 3.6 wt%, respectively. This suggests that Pt is more easily and strongly bonded to the MoS $_2$ support than to WS $_2$. Similarly, in Mo-W-S based catalyst, Pt loading was consistently higher using the WIR method (8.1 wt% for 2D and 8.7 wt% for 3D supports) compared to the MW method (7.5 wt% for 2D and 6.4 wt% for 3D supports). The lower Pt loadings obtained using the MW method, compared to the WIR method, may be attributed to the significantly shorter impregnation time. While the WIR process allows nearly 24 hours for metal incorporation, the MW method was completed within only 25 minutes, which may limit the extent of platinum deposition onto the support. In addition, platinum losses were observed during the catalyst filtration and washing steps which discussed below.



Table 2: XRF results for Pt supported on bulk and nanosheet analogues of MoS₂, WS₂, Mo-W-S

Catalyst	XRF Elemental Composition (wt%)				
	Pt	Mo	W	S	Other
MoS ₂	-	54	-	29	16
Pt/2D-MoS ₂ -MW	10.5	52	0	26	11
Pt/2D-MoS ₂ -WIR	10.5	52	0	27	10
Pt/3D-MoS ₂ -MW	10.0	50	0	26	11
Pt/3D-MoS ₂ -WIR	10.5	52	0	25	11
WS ₂	-	-	75	24	x
Pt/2D-WS ₂ -MW	3.6	0	73	23	x
Pt/2D-WS ₂ -WIR	9.0	0	71	20	x
Pt/3D-WS ₂ -MW	1.2	0	77	21	x
Pt/3D-WS ₂ -WIR	8.7	0	76	16	x
Pt/2D-MoW-S-MW	7.5	10	59	23	x
Pt/2D-Mo-W-S-WIR	8.1	10	59	23	x
Pt/3D-Mo-W-S-MW	6.4	10	60	23	x
Pt/3D-Mo-W-S-WIR	8.7	10	59	22	x

Along with main elements, other elements were also detected by XRF. Si content up to 6.7 wt% and Mg content around 1.5 wt% were detected in case of using MoS₂ as the support. These elements are taken as the impurities of the supporting material originating from its preparation. Other elements including Ca, Fe, Cu, Pb and Al were detected in small amounts below 1wt%.

To further validate the catalyst composition, SEM/EDS analysis was performed. EDS confirmed the presence of Pt NPs via a peak at approximately ~2.2 keV which is in line with earlier literature⁴². In comparison with the XRF measurements, EDS showed slightly lower Pt contents, which was expected because EDS interrogates a smaller, surface-localized volume than XRF. Even so, the EDS data were consistent with the XRF trends, reproducing the same relative differences in Pt loadings. Additional information obtained using SEM analysis are discussed below.

Inductively Coupled Plasma Optical Emission Spectrometer (ICP-OES)

During the catalyst preparation, a filtration step was used to separate the solid catalyst from the liquid phase. The resulting filtrate was analyzed by ICP-OES to determine whether any platinum (Pt) remained in solution. The analysis showed that part of the Pt remained dissolved, with concentration of 1.21 mg/L (RSD 4.92 %), indicating incomplete deposition of Pt onto the TMD support. This result explains the lower Pt content observed in the XRF analysis of several samples, confirming that not all Pt was successfully anchored and that some fraction remained in the impregnation solution. The ICP-OES data therefore corroborate the XRF findings. Notably, this issue was mainly observed for catalysts prepared via the microwave-assisted method, whereas catalysts synthesized by the incipient wetness method exhibited minimal platinum losses.

Atomic Absorption Spectrometry (AAS)

View Article Online
DOI: 10.1039/D5CY01520K

After filtration, the catalyst retained on the filter paper was rinsed three times with distilled water (3 x 10 mL) to remove any soluble residues. The combined washings were analyzed by AAS to assess potential Pt loss during the washing step. The results confirmed that only a small amount of Pt was leached from the support with Pt concentrations in the wash water remaining below 0.7 mg/L, indicating that washing contributed only minimally to overall Pt losses.

When combining the Pt mass balance from all analytical methods, XRF (Pt anchored on the support), ICP-OES (Pt remaining in the impregnation solution), and AAS (Pt present in the washing water), the overall Pt recovery exceeds 90%. Considering the measurement uncertainties of all three techniques, the Pt mass balance can be regarded as closed, indicating that all Pt not immobilized on the support remains dissolved in the liquid phase.

Scanning Electron Microscopy (SEM)

The surface morphology of all prepared catalysts was examined using scanning electron microscopy (SEM) equipped with a backscattered electron (BSE) detector. Representative SEM images of the Pt-supported on bulk forms of TMDs catalysts are shown in **Figure 2** and in the Supplementary Data file (**Fig. S1 a-i**). Some dark regions and bright particles are visible in certain images; however, it is difficult to determine whether these features correspond to Pt nanoparticles. No significant differences were observed between the catalysts prepared by different methods or between the bulk and exfoliated supports. **Figure 2(a-c)** displays SEM images of Pt nanoparticles supported on pure bulk materials MoS₂ and WS₂ and their composite Mo-W-S synthesized via WIR method.

Transmission Electron Microscopy (TEM)

TEM analysis was used for more detailed study of Pt NPs morphology and size. The TEM images and Pt particles size distributions are presented in **Figure 3** confirm the successful deposition of Pt nanoparticles on all TMD supports, appearing as dark, quasi-spherical domains uniformly dispersed across the support surface. Despite high Pt loadings (up to 9.2 wt%), no severe agglomeration or large cluster formation was observed.

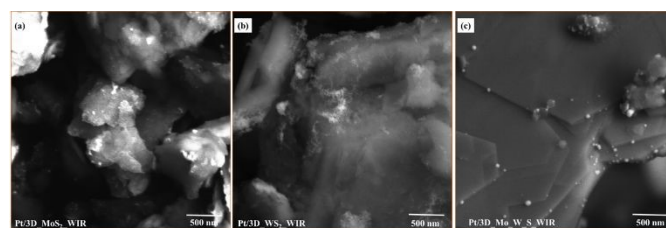


Figure 2: SEM images of (a) Pt/3D-MoS₂ WIR, (b) Pt/3D-WS₂ WIR and (c) Pt/3D-Mo-W-S WIR



MoS₂-supported catalysts shown in **Figures 3(a–d)** exhibited the narrowest particle size distributions (2–10 nm). Pt/2D-MoS₂-MW contained the smallest particles, with ~70 % in the 2–4 nm range, while other MoS₂ samples displayed ~80 % between 2–6 nm, with minor populations up to 9 nm. All particles were predominantly spherical.

TEM analysis of WS₂-supported catalysts demonstrated in **Figures 3(i–l)** revealed pronounced support effects. The exfoliated 2D variants (Pt/2D-WS₂-WIR, Pt/2D-WS₂-MW) contained predominantly particle ranging between 2 and 6 nm, with only small fractions extending to 8–12 nm. In contrast, bulk WS₂ contained broader distribution Pt NPs sizes. Pt/3D-WS₂-MW catalysts was enriched in the 4–8 nm range, whereas Pt/3D-WS₂-WIR shifted toward larger particles (12–20 nm). But it should be noted here that much lower Pt

loading was determined for Pt/3D-WS₂-MW catalyst being only 1.2 wt%. These results further confirm our conclusion that Pt interacts less strongly with WS₂ than with MoS₂, leading to lower Pt loading efficiency and the formation of larger Pt NPs when WS₂ is used as the support. TEM images of Mo-W-S composites-based catalysts are presented in **Figures 3(q–t)**. Microwave-assisted synthesis yielded finer, more uniform dispersions than WIR. Pt/2D-Mo-W-S-MW was sharply centred at 4–6 nm (>70% population), while WIR-derived samples exhibited broader distributions (2–14 nm).

Overall, usage of exfoliated 2D supports and microwave-assisted synthesis promoted smaller, more homogeneously dispersed Pt NPs, whereas 3D supports and WIR methods led to broader distributions and partial agglomeration.

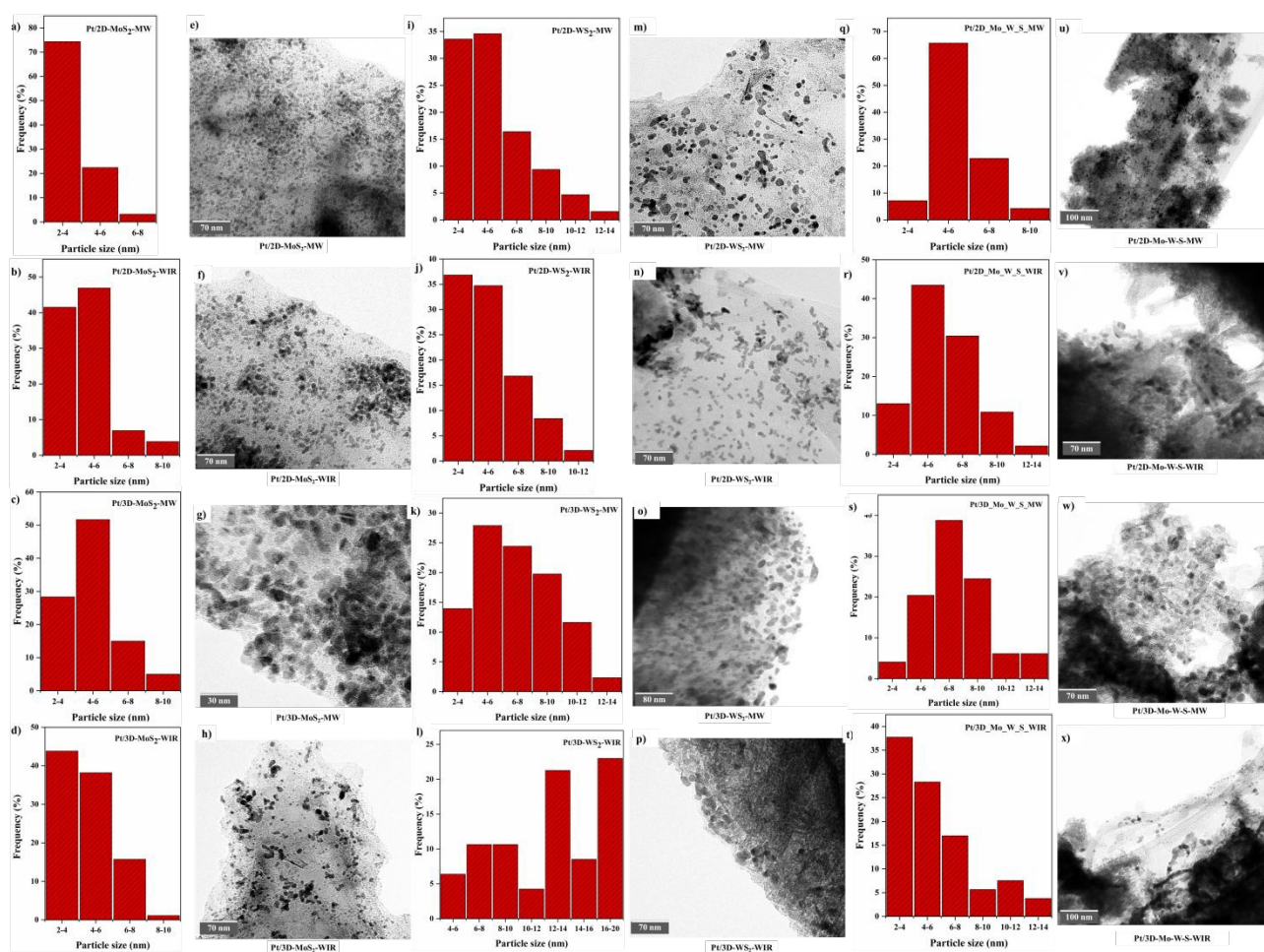


Figure 3: Comparative TEM study: Particle size distribution of MoS₂ based catalyst (a-d) and their corresponding TEM images (e-h), particle size distribution of WS₂ based catalyst (i-l) and their corresponding TEM images (m-p), particle size distribution of Mo-W-S based catalyst (q-t) and their corresponding TEM images (u-x).



X-ray Diffraction (XRD)

The crystalline structures of the prepared catalysts were investigated using X-ray diffraction (XRD). **Figure 4** compares the patterns of pristine 3D-MoS₂ and its 2D counterpart. Both exhibited sharp reflections characteristic of the hexagonal MoS₂ phase, with the dominant (002) peak at 14.4° 2θ (ICCD card No. 37-1492)^{43,44}. In the 2D-MoS₂ sample, the persistence of this (002) reflection together with the attenuation of secondary peaks confirms the formation of few-layer nanosheets with reduced c-axis stacking.

Catalyst diffractograms closely resembled those of their pristine MoS₂ supports. Notably, 2D-MoS₂-WIR displayed sharper peaks relative to pristine 2D-MoS₂, suggesting partial restacking of the material layers and improved long-range order, consistent with the structural rearrangements often observed upon impregnation. Importantly, no distinct Pt reflections were detected in any MoS₂-supported catalysts, indicating that Pt nanoparticles remained highly dispersed and below the XRD detection threshold. This observation aligns with previous reports, where even at ~8 wt% Pt loading, diffraction peaks were absent due to the nanoscale particle dimensions and uniform dispersion⁴⁵.

Figure 5 presents the XRD patterns of Pt-loaded catalysts supported on 3D-WS₂ and its 2D analogues. For bulk WS₂, intense reflections were observed at 14.2°, 28.6°, 32.6°, 33.4°, 39.6°, 44.0°, 49.6°, 58.2°, 60.0°, 60.3°, 66.7°, and 76.0° 2θ, corresponding to the (002), (004), (100), (101), (103), (006), (105), (110), (008), (112), (114), and (116) planes of the hexagonal WS₂ phase (JCPDS 00-08-0237)⁴⁶. In contrast, the 2D-WS₂ nanosheets exhibited only a single reflection at ~14.2° 2θ, indexed to the (002) plane, consistent with monolayered or few-layered structures reported in literature⁴⁷. Pt/3D-WS₂ catalysts retained the major features of the bulk support but exhibited two additional peaks at 23.9° and 35.8° 2θ (denoted in **Figure 5** by *), which are absent in pristine WS₂ and likely arise from partial oxidation during preparation. These are consistent with low-crystallinity WO₃, which typically exhibits a cluster of reflections at 23°–24° 2θ (JCPDS 20-1324)^{48,49}. The appearance of WO₃-related peaks is attributed to partial oxidation of the WS₂ support during catalyst preparation. XRF analysis indicates a decrease in sulfur content after Pt deposition, specifically in the Pt/3D-WS₂-WIR catalyst the sulfur content decreased to ~16 wt%, compared with ~24 wt% for the pristine support, and in XRD results this catalyst showed prominent appearance of WO₃ peak. Sulfur depletion is consistent with the formation of S vacancies, which create under-coordinated W sites and increase the susceptibility of the material to oxidation. Consequently, these defect sites can promote partial conversion of the sulfide phase to WO₃, giving rise to the observed WO₃ signals.

In comparison with the pure supports, two additional weak peaks were observed in pattern of Pt/3D-WS₂-WIR at 46.3° 2θ (200) and 67.8° 2θ (220), which correspond to metallic Pt nanoparticles (JCPDS 04-0802). This result is in good agreement with the TEM analysis, which indicated the presence of the largest Pt nanoparticles among all the prepared catalysts. For

catalysts derived from 2D-WS₂ supports, partial restacking of nanosheets was evident, as weaker but discernible peaks appeared at the same positions as bulk WS₂. This phenomenon, commonly reported in literature^{50–52} is attributed to solvent removal during drying, which enables van der Waals-driven reaggregation of exfoliated layers. As shown in **Figure 6**, all Mo-W-S composite preserved the 2H-layered structure, with reflections assignable to both MoS₂ and WS₂ phases. The peaks were generally broader and less intense than those of the pure phases, indicative of reduced crystallinity due to Mo/W lattice mixing. Bulk samples displayed sharper reflections, consistent with larger crystallites. In all cases, the (002) reflection near 14° 2θ remained prominent. Catalyst samples also exhibited additional peaks, in Pt/3D-Mo-W-S-MW, a peak marked (*) was observed, attributed to partial WS₂ oxidation, while a weak reflection at 67.5° 2θ corresponding to Pt(220) confirmed the presence of metallic Pt nanoparticles.

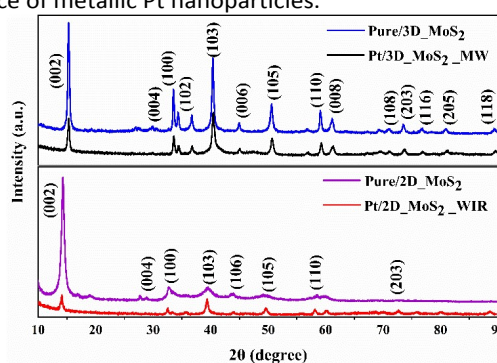


Figure 4: XRD patterns of pure MoS₂ supports and MoS₂ based catalyst.

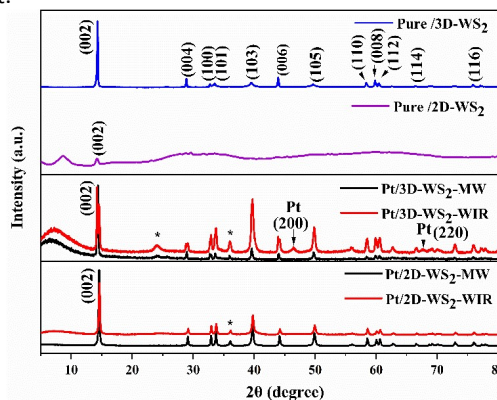


Figure 5: XRD patterns of pure WS₂ supports and WS₂ based catalyst.

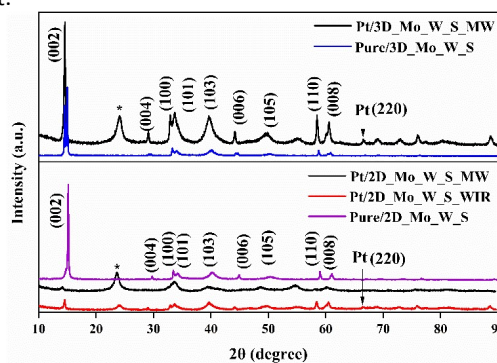


Figure 6: XRD patterns of pure Mo-W-S supports and Mo-W-S based catalysts.



Nitrogen physisorption

Nitrogen physisorption method was used to calculate the BET surface areas of Pt-supported catalysts prepared on 3D-MoS₂, 3D-WS₂, and 3D-Mo-W-S supports using both the WIR and MW methods and the results are summarized in the supplementary data file (Table S2). There was significant effort to determine values for specific surface areas also for 2D analogues of the tested supports, however the method was developed for porous materials and therefore it gives unreproducible results for materials with only apparent porosity given by interlayer spacing. For the MoS₂-based catalysts, the surface areas were 27 m²/g (Pt/3D-MoS₂-WIR) and 21 m²/g (Pt/3D-MoS₂-MW) indicating that the surface areas remain relatively low and do not vary much between treatments. In contrast, the WS₂-supported catalysts showed the highest variation, with Pt/3D-WS₂-MW exhibiting a significantly larger surface area (58 m²/g) compared to Pt/3D-WS₂-WIR (20 m²/g). In the case of the Mo-W-S composite supports, the MW-prepared catalyst had a moderate surface area of 22 m²/g, while the WIR-prepared catalyst displayed the lowest value (5 m²/g). In particular, the MW method generally enhanced surface area compared to WIR for WS₂ and the Mo-W-S composite, whereas the difference was less pronounced for MoS₂-based systems.

Photoelectron spectroscopy

High-resolution X-ray photoelectron spectroscopy (XPS) was conducted to elucidate the surface chemical states of Pt/3D-MoS₂-MW, Pt/2D-WS₂-MW, and Pt/Mo-W-S in both 2D and 3D architectures. For Pt/3D-MoS₂-MW, the Mo 3d spectrum is dominated by Mo⁶⁺ peaks located at ~234.5 eV (3d_{5/2}) and ~237.6 eV (3d_{3/2}), indicating pronounced surface oxidation of molybdenum (Fig. 7a). Minor contributions at ~230.8 and ~233.9 eV correspond to Mo⁴⁺, suggesting that only a small fraction of Mo remains in the sulfide state. The S 2p spectrum is primarily composed of S–O components at ~169.5 eV (2p_{3/2}) and ~170.7 eV (2p_{1/2}), while weak doublets at ~163.3 and ~164.5 eV are assigned to sulfide (S²⁻) species, confirming substantial sulfur oxidation. In the Pt 4f region, metallic Pt⁰ appears at ~71.2 eV (4f_{7/2}) and ~74.5 eV (4f_{5/2}), whereas the dominant contribution arises from Pt²⁺ (~72.6 and ~75.9 eV), accompanied by weaker Pt⁴⁺ peaks (~74.2 and ~77.5 eV), indicating that Pt predominantly exists in an oxidized state.

For Pt/2-WS₂-MW, the W 4f spectrum shows dominant W⁴⁺ doublets at ~36.5 eV (4f_{7/2}) and ~38.6 eV (4f_{5/2}), confirming that tungsten largely retains its sulfide state (Fig. 7b). Minor W⁶⁺ features at ~37.3 and ~39.4 eV indicate limited surface oxidation. Similar to the Mo-based sample, the S 2p region is dominated by S–O species (~169.4 and ~170.6 eV), with minor sulfide contributions (~162.5 and ~163.7 eV). The Pt 4f spectrum is mainly composed of Pt²⁺ (~72.5 and ~75.8 eV), with

smaller amounts of metallic Pt⁰ (~71.1 and ~74.4 eV) and Pt⁴⁺ (~74.0 and ~77.2 eV). DOI: 10.1039/D5CY01520K

For the mixed Pt/2D-Mo-W-S-MW system (Fig. 7c), the Mo 3d spectrum is again dominated by Mo⁶⁺ species with only weak Mo⁴⁺ contributions, indicating that Mo remains highly susceptible to surface oxidation. In contrast, the W 4f region exhibits predominantly W⁴⁺ with minor W⁶⁺ components, demonstrating that tungsten preserves the sulfide framework more effectively. The S 2p spectrum is largely composed of S–O signals with minor S²⁻ contributions, reflecting substantial surface sulfur oxidation. In this case, the Pt 4f region is dominated by metallic Pt⁰, accompanied by minor Pt²⁺ and Pt⁴⁺ components, suggesting that Pt is primarily present in a reduced metallic state.

For the Pt/3D-Mo-W-S-MW architecture (Fig. 7d), the Mo 3d spectrum remains Mo⁶⁺-rich with only trace Mo⁴⁺, confirming extensive surface oxidation of Mo. The W 4f region is still dominated by W⁴⁺ with minor W⁶⁺ contributions, indicating preservation of tungsten in the sulfide state. The S 2p spectrum is mainly composed of S–O species with minor sulfide signals, consistent with partial surface oxidation. Notably, the Pt 4f spectrum shows comparable contributions from Pt⁰ and Pt²⁺, along with a minor Pt⁴⁺ fraction, indicating a higher proportion of interfacial or partially oxidized Pt species compared to the 2D mixed phase.

The XPS results show clear trends in surface chemistry: Mo-containing samples exhibit predominantly Mo⁶⁺ surface species, whereas W largely remains in the W⁴⁺ sulfide state. Sulfur is significantly oxidized at the surface in all materials, as indicated by dominant S–O signals. The Pt oxidation state varies with composition and architecture: Pt²⁺ dominates in Pt/MoS₂ and Pt/WS₂, metallic Pt⁰ is prevalent in 2D Pt/2D-Mo-W-S system, and a mixed Pt⁰/Pt²⁺ state appears in the 3D mixed catalyst. These trends suggest that W incorporation stabilizes the sulfide framework and promotes metallic Pt, while the 3D architecture enhances metal–support interactions and facilitates partial Pt oxidation or interfacial charge redistribution.

Importantly, XRD detected WO₃ formation only in samples that did not undergo XPS analysis (e.g., Pt/3D-WS₂). This indicates that bulk oxidation of WS₂ to WO₃ occurred during storage or handling, but was not present in the specific samples analyzed by XPS. Since XPS probes only the top ~5 nm, it is highly sensitive to surface oxidation (S–O, Mo⁶⁺), whereas XRD detects bulk crystalline phases. The absence of MoO₃ reflections in MoS₂-based samples confirms that MoS₂ retained its hexagonal structure, with no detectable bulk oxidation. Together, these results show that surface oxidation is widespread and captured by XPS, while bulk oxidation (WO₃ formation) is sample-dependent and only observed by XRD in materials not analyzed by XPS. The two techniques therefore provide complementary information rather than contradictory results.



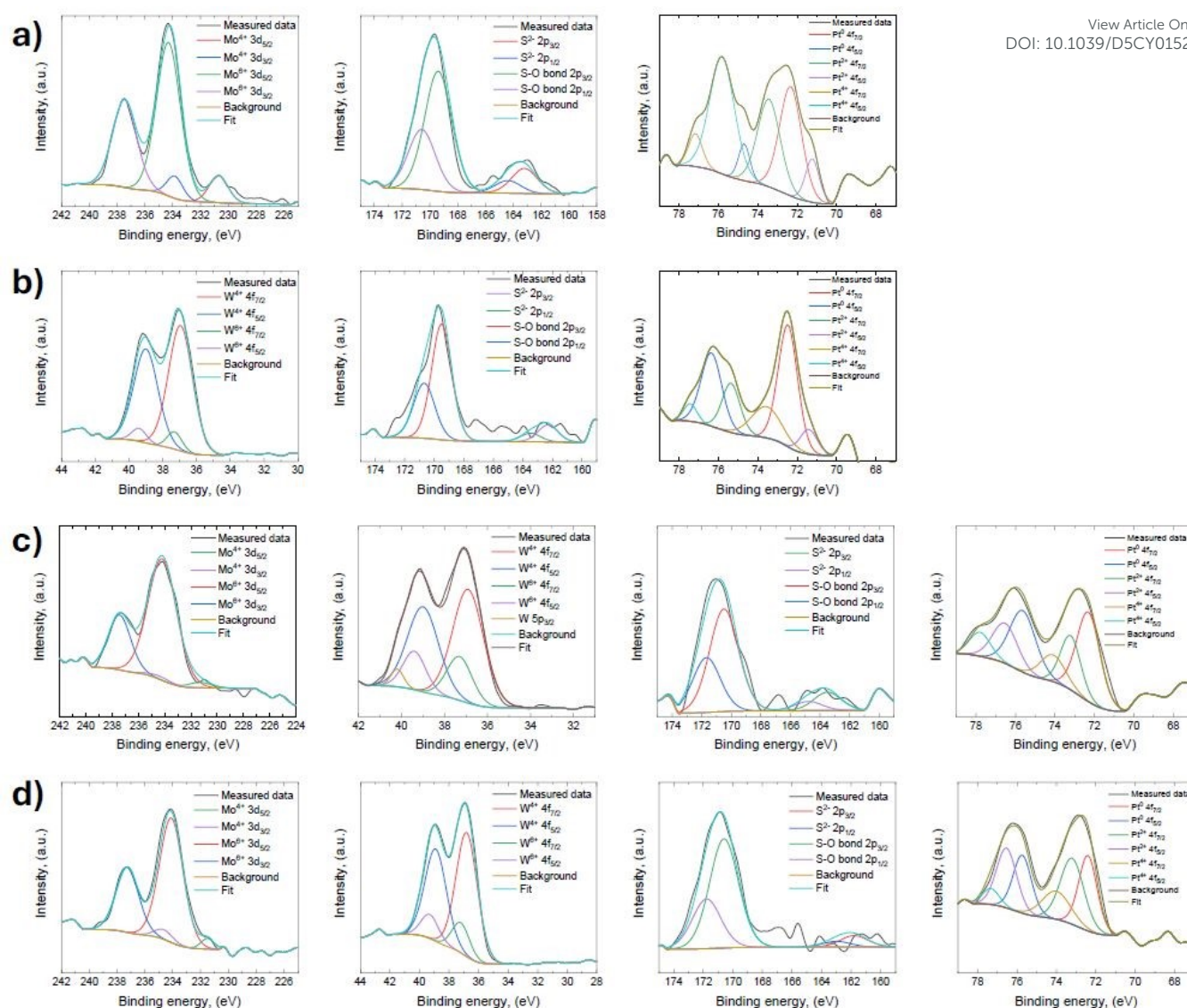


Figure 7: XPS high-resolution Mo3d and/or W4f, S2p and Pt4f spectra of (a) Pt/3D-MoS₂-MW, (b) Pt/2D-WS₂-MW, (c) Pt/2D-Mo-W-S-MW and (d) Pt/3D-Mo-W-S-MW

Catalytic testing: Cinnamaldehyde hydrogenation

Catalyst Activities: Conversion of Cinnamaldehyde. The catalytic performance of the prepared materials evaluated in cinnamaldehyde (CAL) hydrogenation is summarized in **Figure 8** as a function of conversion in reaction time. In all cases, conversion increased monotonically with time, though pronounced activity differences were evident across catalytic systems. The nature of the support exerted the dominant influence, with Mo-W-S consistently outperforming both MoS₂ and WS₂. Composite-supported catalysts achieved the highest overall conversions (~70–75 % within 360 min), while bulk supports were systematically less active than their 2D analogues. **Figure 8a**, presents the results obtained using MoS₂-supported catalysts. Pt/2D-MoS₂-WIR exhibited the highest activity, reaching ~18 % conversion at 60 min and ~59 % at 360 min, clearly surpassing bulk-MoS₂-based systems. This

enhancement is attributed to improved Pt dispersion and greater accessibility of active sites in the 2D structure. A similar trend was observed for WS₂-supported catalysts (presented in **Figure 8b**), albeit with higher overall conversions. Pt/2D-WS₂-WIR displayed rapid initial activity (~23 % at 60 min) and attained ~63 % conversion at 360 min, while Pt/2D-WS₂-MW reached ~52 % at the same time. By contrast, bulk WS₂ catalysts remained significantly less active, with maximum conversions below 40 % after 360 min. **Figure 8c** demonstrates achieved CAL conversions using Mo-W-S composites-based catalyst. These catalysts exhibited the most promising catalytic behaviour. Pt/2D-Mo-W-S-MW achieved ~29 % conversion at 60 min and ~75 % at 360 min, closely followed by Pt/2D-Mo-W-S-WIR (~70 % at 360 min). Even the bulk composites outperformed bulk MoS₂ and WS₂, underscoring the intrinsic advantage of Mo–W composite.



To gain insight into the reaction progress, the reaction rates and turn over frequencies were determined for all tested catalysts and Table 3 shows a detailed comparison of these values. The rates were calculated with consideration of the Pt NPs loading (XRF data) and mass of catalyst used in reaction. While in TOF calculation Pt dispersion on surface was used which was calculated using average particles size obtained from TEM analysis. The initial reaction rates were derived from CAL concentrations measured between 0-30 min. Although this time interval is relatively long, the recorded conversions remained below 25 %, indicating that the reactions proceeded within the initial kinetic regime. Overall, the initial reaction rates were consistently higher than the rates observed at higher reaction times, reflecting a decline in activity as the reaction progressed. Among the MoS₂-based catalysts, the Pt/2D-MoS₂-WIR exhibited the highest initial as well as final reaction rates compared to other MoS₂-based systems. Also, this catalytic system showed the highest TOF and showed good alignment with obtained rate of reactions. These findings are consistent with the conversion profiles presented in Figure 8.

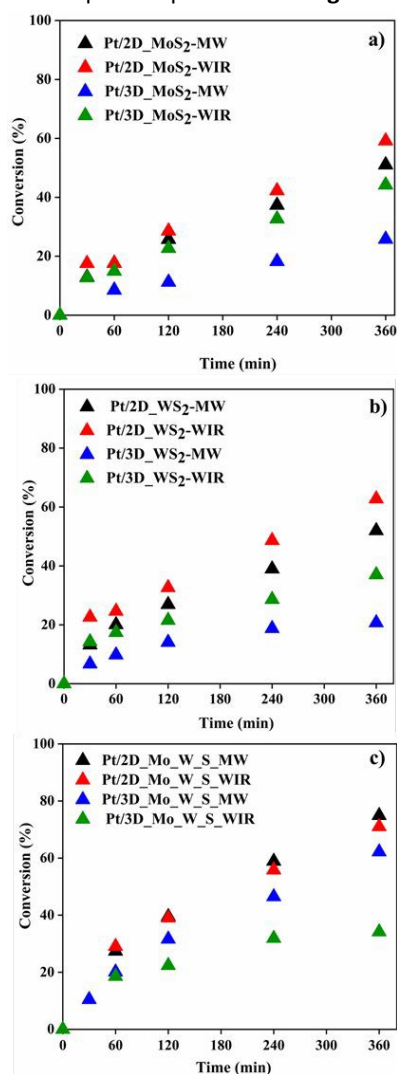


Figure 8: CAL conversion as a function time using different catalytic systems: (a) Pt/MoS₂ (b) Pt/WS₂ and (c) Pt/ Mo-W-S

For the WS₂-based catalysts, the reaction rates normalized to catalyst mass demonstrate that catalysts with lower Pt loadings exhibited the highest initial reaction rates. For instance, 3D-WS₂-MW, with the lowest Pt loading of 1.2 wt%, displayed the highest initial rate among all tested catalysts being $14.1 \cdot 10^{-2}$ mmol·min⁻¹·mg_{Pt}⁻¹. A similar trend was observed for the 2D-WS₂-based catalysts. TOF data was also consistent with these findings. This behaviour is attributed to the fact that, at lower loadings, a larger fraction of Pt nanoparticles actively participated in the catalytic process. Similarly in Mo-W-W based system, catalyst containing lower Pt loading 6.4 wt% exhibited higher TOF $3.7 \cdot 10^{-1} \text{ s}^{-1}$ and the highest final reaction rates. The subsequent decline in reaction rates suggests either partial catalyst deactivation or the saturation of active sites. However, regardless of the loading, catalytic activity was strongly limited at longer reaction times. Overall, among all the studied catalysts, higher rates of reaction were observed among 2D-supported catalyst compared to the bulk-supports. It is obvious that exfoliated supports exhibit higher exposed surface and defect sites which enhance the probability of reactant adsorption and reaction compared to bulk, less defective surfaces⁵³.

Selectivities toward hydrogenation and side products. The selectivities toward cinnamyl alcohol (COL), hydrocinnamaldehyde (HCAL), and hydrocinnamyl alcohol (HCOL) obtained over Pt-supported catalysts were evaluated as a function of CAL conversion. Next to the listed products of hydrogenation one side product was detected using GC. GC-MS analysis confirmed the side product as 3-isopropoxy-propan-1-yl benzene (named "ETHER"), formed via reductive etherification of CAL with isopropanol under reaction conditions, consistent with previous reports⁴⁰.

COL, the product of carbonyl group hydrogenation, was the main product obtained using all tested catalysts and its selectivity was increasing with increasing of CAL conversion in all presented hydrogenation experiments. HCAL, the aldehyde with hydrogenated olefinic double bond, was produced in significantly smaller amounts, with selectivities toward HCAL remaining below 10 %. Additionally, the presence of HCOL, the product of hydrogenation of both olefinic and carbonyl double bonds, HCOL formation was minimal ($\leq 5\%$) and absent in the bulk-MW catalyst. At early stages, COL and ether were formed competitively, but COL became dominant as the reaction progressed. Figure 9 (a-d) present selectivities obtained over MoS₂-supported catalysts. COL selectivities up to 60% were achieved using all MoS₂-based catalysts. Results obtained over WS₂-supported catalysts presented in Figures 9 (e-h) demonstrated COL as dominant product with the highest selectivity (54%) observed for Pt/2D-WS₂-WIR. Ether was consistently formed as a side product, with selectivity reaching 28% in 2D-based catalysts and up to 43% in bulk catalysts at low conversions before decreasing as COL formation increased. Other hydrogenated products HCAL and HCOL remained below 10%. In Pt/3D-WS₂-MW, COL selectivity was poor (<32%), with ether as the main product and HCOL reaching 20% at low conversion level.



Table 3: Rate of reactions achieved over tested catalysts

Catalyst	CAL conversion (%)	XRF Pt loading (wt.%)	r_0 (mmol·min ⁻¹ mg _{Pt} ⁻¹)*(10 ⁻²)	r_t (mmol·min ⁻¹ mg _{Pt} ⁻¹)*(10 ⁻²)	Average Pt size from TEM (nm)	TOF (s ⁻¹)*(10 ⁻¹)
Pt/2D-MoS ₂ -MW	51	10.5	3.5	0.9	3.9	1.2
Pt/2D-MoS ₂ -WIR	59	10.5	4.9	1.1	4.5	1.6
Pt/3D-MoS ₂ -MW	26	10.0	1.4 ^α	0.5	4.9	0.8
Pt/3D-MoS ₂ -WIR	44	11.1	4.6	0.8	3.6	0.7
Pt/2D-WS ₂ -MW	52	3.6	9.2	2.5	5.5	4.3
Pt/2D-WS ₂ -WIR	63	9.0	6.2	1.0	5.1	1.8
Pt/3D-WS ₂ -MW	21	1.2	14.1	2.7	6.7	5.9
Pt/3D-WS ₂ -WIR	37	8.7	4.2	0.6	14.4	2.7
Pt/2D-Mo-W-S-MW	75	7.5	4.4 ^α	1.5	5.4	2.7
Pt/2D-Mo-W-S-WIR	71	8.1	4.6 ^α	1.3	5.9	2.8
Pt/3D-Mo-W-S-MW	62	6.4	4.1	1.8	7.7	3.7
Pt/3D-Mo-W-S-WIR	34	8.7	2.7 ^α	0.5	5.2	0.5

α = 60 min. r_0 = initial reaction rates (0 – 30 min), r_t = reaction rate between (30 – 360 min); reaction conditions (CAL, isopropyl alcohol, 80 °C, 1 MPa, 6 h)

As it was observed in XRD that additional diffraction peaks corresponding to WO₃ were observed only for the bulk-supported catalyst, whereas they are absent for the 2D-supported catalyst. Notably, the bulk-supported catalyst also exhibits a higher ether selectivity compared with the 2D-supported catalyst. Since the ether product is primarily associated with the solvent-derived pathway, these observations suggest that the WO₃ phases present in the bulk-supported catalyst facilitate ether formation, thereby enhancing the observed selectivity.

For Mo-W-S-supported catalysts (Figures 9 (i-l)), COL was the dominant product, with selectivity increasing as conversion proceeded. The highest COL selectivity (64.3 %) was obtained for the 2D-MW catalyst. Across all composites, COL selectivity exceeded 40 %. At low conversions, ether was formed competitively but remained below 23 %, except for the bulk-WIR catalyst, which reached 30 % and showed no HCOL formation. HCOL and HCOL selectivities remained consistently low (<8 %) and its formation was rather constant during whole reaction time. The Mo-W-S system particularly in 2D nanosheet form (MW or WIR) achieved the best balance of high activity and high COL selectivity.

Additionally, product selectivities toward the primary hydrogenation products COL, HCOL and HCOL as well as by product ether were determined at 10% and 30% CAL conversion levels for all catalysts, as detailed in Table 4. Selectivities toward minor, unidentified byproducts formed in small amounts are also reported to provide a complete picture of the product distribution under the given reaction conditions. Yield of hydrogenation products were also calculated as a function of time and obtained results are shown in supplementary file S4.

As discussed above, COL selectivities increased with increasing CAL conversion and the highest COL selectivities at 30 % conversion levels exceed 50 % using all 3D-based supports independently on their chemical composition. The final CAL conversions, COL selectivities and COL yields obtained within

360 minutes of the reaction are described in Table 5. Among all, Pt/2D-Mo-W-S-MW showed the best results, with the highest CAL conversion (75 %), COL selectivity (64 %), and COL yield (48 %).

Its counterpart prepared by conventional impregnation, Pt/2D-Mo-W-S-WIR, also performed well (71 % CAL conversion, 61 % COL selectivity, 43 % COL yield). In contrast, bulk (3D) catalysts generally exhibited lower activity and yields, confirming that 2D supports outperform 3D forms in the catalytic activity.

However, the higher selectivities toward COL (at 30 % conversion level) are achieved using bulk forms of supports but in combination with lower achieved CAL conversions, the final COL yields are lower. Additionally, Mo-W composite supports consistently outperformed pure MoS₂ and WS₂, highlighting the advantage of combined composition and 2D morphology for both activity and selectivity.

To further verify the possible reason for formation of ether two additional control reactions were performed under identical reaction conditions, one using the pure MoS₂ support without Pt loading and the other employing a commercial Pt/Al₂O₃ catalyst. In the MoS₂-based system (without Pt), a CAL conversion of 6 % was observed. The product distribution showed 27 % selectivity toward HCOL, 4.7 % toward HCOL, 38 % selectivity toward ether, and 31 % selectivity toward additional side products. When the reaction was carried out using commercial 5 % Pt/Al₂O₃ resulted 16 % conversion with 38 % selectivity toward HCOL, 25 % toward COL, and 5 % toward HCOL. Ether selectivity reached 18 %, while additional side products selectivity was 15 %. The formation of ether in both catalytic systems indicates that ether production is not exclusively associated with a specific support material, nor can it be attributed solely to the acidity of the support. Instead, these findings suggest that solvent chemistry played a role in ether formation. As discussed previously, this behavior is most likely related to the participation of isopropyl alcohol in a reductive etherification pathway.



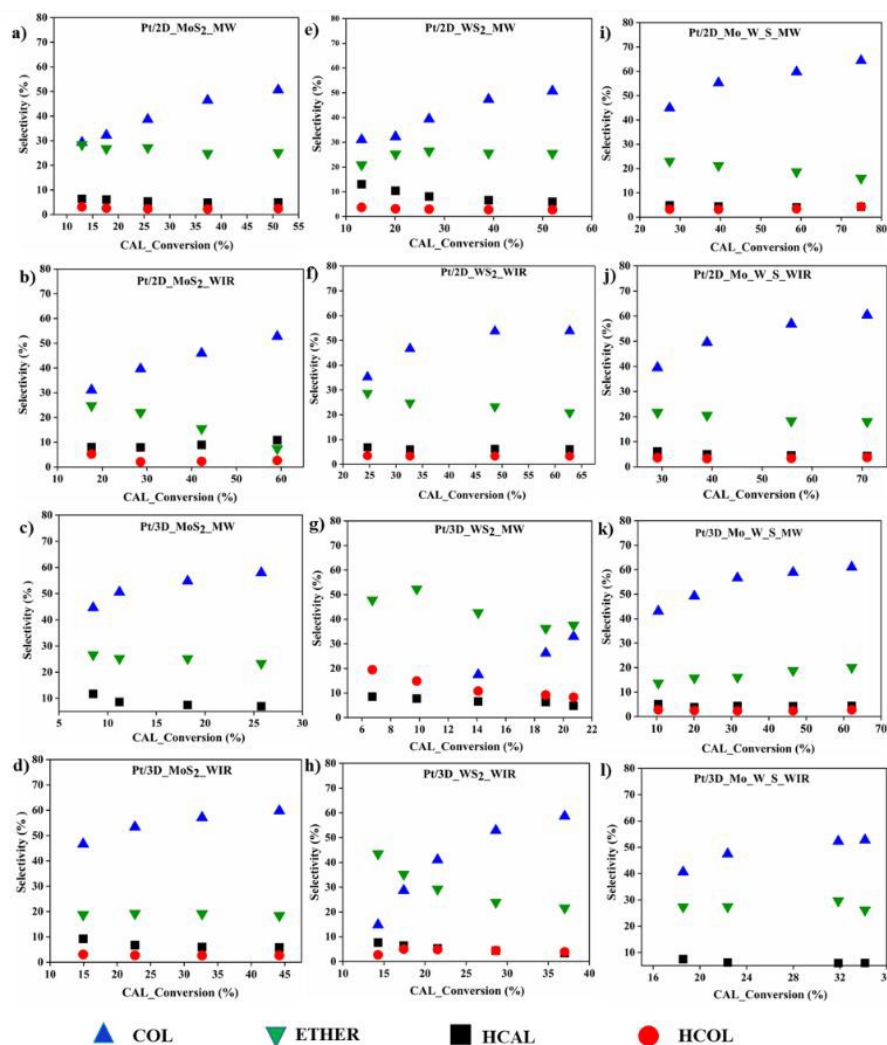


Figure 9: Selectivities of CAL hydrogenated products (HCAL, HCOL, COL) as a function of CAL conversion obtained using prepared catalyst (a-d) MoS₂ based catalyst, (e-h) WS₂ based catalyst (i-l) Mo-W-S based catalyst

Table 4: Selectivities of COL, HCAL and HCOL at 10 % and 30 % CAL conversion

Catalyst	Selectivity at 10%/30% Conversion of CAL (%)											
	COL		HCAL		HCOL		Ether		Other		Sum of H ₂ Products	
	10%	30%	10%	30%	10%	30%	10%	30%	10%	30%	10%	30%
Pt/2D-MoS ₂ .MW	29.3	38.6*	6.4	5.3*	3.1	2.3*	28.4	27.2*	32.8	26.6*	38.8	46.2*
Pt/2D-MoS ₂ .WIR	31.0 [¥]	39.6 ^c	8.0 [¥]	8.0 ^c	5.2 [¥]	2.1 ^c	24.8 [¥]	22.0 ^c	31.0 [¥]	28.3 ^c	44.2 [¥]	49.7 ^c
Pt/3D-MoS ₂ .MW	50.5	57.9*	8.6	7.0*	0	0	25.2	23.4*	15.7	11.7*	59.1	64.9*
Pt/3D-MoS ₂ .WIR	46.6 [Ⓚ]	57.0	9.2 [Ⓚ]	5.9	3.1 [Ⓚ]	2.6	18.7 [Ⓚ]	19.1	22.4 [Ⓚ]	15.4	55.8 [Ⓚ]	65.5
Pt/2D-WS ₂ .MW	31.0	39.3 ^c	13.0	8 ^c	3.7	3 ^c	21	26.4 ^c	31.3	23.3 ^c	47.7	50.3 ^c
Pt/2D-WS ₂ .WIR	0 [Ⓟ]	46.6	9.8 [Ⓟ]	6.1	0 [Ⓟ]	3.3	49 [Ⓟ]	24.7	41.2 [Ⓟ]	19.3	9.8 [Ⓟ]	56.0
Pt/3D-WS ₂ .MW	0	33 [£]	7.7	4.8 [£]	14.9	8.3 [£]	52.3	37.6 [£]	25.1	16.3 [£]	22.6	46.1 [£]
Pt/3D-WS ₂ .WIR	14.8 [Ⓚ]	53.0 [Ⓟ]	7.6 [Ⓚ]	4.4 [Ⓟ]	2.7 [Ⓚ]	4.4 [Ⓟ]	43 [Ⓚ]	24 [Ⓟ]	31.8 [Ⓚ]	14.2 [Ⓟ]	25.1 [Ⓚ]	61.8 [Ⓟ]
Pt/2D-Mo-W-S-MW	-	44.9 [Ⓟ]	-	4.8 [Ⓟ]	-	3.3 [Ⓟ]	-	23 [Ⓟ]	-	24 [Ⓟ]	-	53 [Ⓟ]
Pt/2D-Mo-W-S-WIR	-	39.4	-	6	-	3.6	-	21.6	-	29.4	-	49
Pt/3D-Mo-W-S-MW	43.0	56.6	5.0	4.3	2.7	2.3	13.7	16.1	35.6	20.7	50.7	63.2
Pt/3D-Mo-W-S-WIR	-	52.2	-	6.0	-	0	-	29.6	-	12.2	-	58.2

Note: (*) = 25 % conversion, (£) = 20 % conversion, (¥) = 17 % conversion, (c) = 28 % conversion, (Ⓟ) = 22 % conversion, (Ⓚ) = 14.5 % conversion, (-) = not recorded (Lowest recorded conversion ≥ 20%), (Ⓚ) = 15 % conversion.



Table 5: Hydrogenation results obtained at 360 min

Catalyst	Results of CAL hydrogenation at 360 min		
	CAL conversion (%)	COL Selectivity (%)	COL Yield (%)
Pt/2D-MoS ₂ -MW	51	51	26
Pt/2D-MoS ₂ -WIR	59	53	31
Pt/3D-MoS ₂ -MW	26	58	15
Pt/3D-MoS ₂ -WIR	44	60	26
Pt/2D-WS ₂ -MW	52	51	26
Pt/2D-WS ₂ -WIR	63	54	34
Pt/3D-WS ₂ -MW	21	33	7
Pt/3D-WS ₂ -WIR	37	59	22
Pt/2D-Mo-W-S-MW	75	64	48
Pt/2D-Mo-W-S-WIR	71	61	43
Pt/3D-Mo-W-S-MW	62	61	38
Pt/3D-Mo-W-S-WIR	34	53	18

Conclusions

Pt-based hydrogenation catalysts supported on the bulk TMDs (MoS₂, WS₂, and Mo-W-S) and their 2D counterparts were synthesized using microwave-assisted and wet impregnation methods, and their performance in cinnamaldehyde (CAL) hydrogenation was evaluated in relation to their physicochemical properties, with particular emphasis on support morphology (2D vs. bulk) and preparation method.

Comprehensive characterization was carried out using SEM/EDS, TEM, XRF, XRD, and BET analyses. SEM/EDS confirmed successful Pt deposition, with most catalysts achieving loadings close to the targeted 9 wt.%, which was validated by XRF. Lower Pt loadings were detected only when WS₂ was used as the support in combination of MW-assisted impregnation method. These results suggest a weaker Pt-WS₂ interaction compared to Pt-MoS₂. Metal losses were clearly observed during the filtration and washing steps. In the case of the microwave-assisted synthesis method, insufficient anchoring of the active metal onto the support surface was evident. This was confirmed by ICP-OES analysis of the filtrate and AAS analysis of the washing solutions, both of which detected measurable concentrations of Pt. These results demonstrate that the portion of platinum not effectively anchored on the support remained dissolved in the impregnation solution, thereby leading to lower Pt loadings determined by XRF compared to the targeted values.

The 2D catalysts favored finer dispersion, with most particles in the 2–6 nm range, while 3D supports showed broader particle size distributions. Microwave-assisted synthesis produced smaller and more uniform nanoparticles compared to wet impregnation, particularly in Mo-W-S systems. In general, smaller and more uniformly distributed nanoparticles correlated with superior catalytic activity.

XRD analysis verified the hexagonal crystal phases of MoS₂ and WS₂, with 2D forms showing reduced secondary peaks

characteristic of few-layer structures. Composite Mo-W-S exhibited broader and less intense reflections, consistent with reduced crystallinity caused by Mo/W mixing. Weak Pt peaks were occasionally detected, reflecting highly dispersed nanoscale Pt particles. Partial oxidation and restacking effects were observed in some cases, particularly in 2D WS₂, likely due to solvent removal during drying, which induced nanosheet collapse.

XPS reveals extensive surface oxidation of Mo and S, partial oxidation of Pt depending on architecture, and greater sulfide stability in W-containing systems.

A strong correlation was observed between surface area, XRD patterns, and CAL conversion for Mo-W-S supported catalysts. Pt/2D-Mo-W-S-WIR exhibited the highest achieved CAL conversion being 75 %, with XRD features showing broader, less intense peaks indicative of increased interlayer spacing and enhanced Pt dispersion. However, surface area alone was insufficient, as adequate Pt loading was also essential, insufficient metal content resulted in reduced activity despite high surface areas.

Catalytic evaluation confirmed that performance in CAL hydrogenation was predominantly governed by support type and size distribution of Pt nanoparticles. Mo-W-S composite, particularly in 2D form, consistently outperformed MoS₂ and WS₂, delivering both the highest activity and the best selectivity toward cinnamyl alcohol (COL). Pt/2D-MoS₂-WIR and Pt/2D-WS₂-WIR outperformed their bulk counterparts, but Mo-W composite nanosheets exhibited superior conversions and selectivity overall. Ether formed via reductive etherification mechanism was detected as a competitive side product at low conversions, especially using bulk catalysts, while HCAL and HCOL remained minor products. Across all systems, Pt-supported TMD catalysts favored selective hydrogenation of the carbonyl (C=O) group over the olefinic (C=C) bond, leading to high COL selectivity. This selectivity was attributed to the ability of well-dispersed Pt on engineered TMD supports to promote C=O chemisorption and activation. Preparation method had only a minor influence compared to the decisive role of support composition and dimensionality.

The most effective catalyst was Pt supported on 2D-Mo-W-S synthesized by the microwave-assisted impregnation method, which achieved 75% CAL conversion after 360 minutes, along with 64.3% selectivity to COL and a 48% its yield. COL selectivity increased progressively with conversion. These findings highlight the strong potential of TMD-based supports, particularly the Mo-W composite in 2D nanosheet form, for the design of efficient catalysts in selective CAL hydrogenation, with 2D structures consistently outperforming their bulk counterparts.

Author contributions

Conceptualization, M.P. and M.V.; methodology, M.P. and M.V.; validation, A.S., M.P., and M.V.; formal analysis, A.S., M.P., I.D., L.K. and M.V.; investigation, A.S., B.S., M.P., I.D., J.L., and L.K.; resources, J.L.; data curation, A.S., M.P., M.V. and I.D.; writing—original draft



preparation, A.S., M.P. and M.V.; writing—review and editing, A.S., and M.P.; visualization, A.S., M.P. and M.V.; supervision, M.P. and M.V.; funding acquisition, M.P. and M.V. All authors have read and agreed to the published version of the manuscript.

Conflicts of interest

The authors declare no conflicts of interest.

Data availability

The data supporting this article have been included as part of the Supplementary Information. Supplementary information: S1: SEM images (a-d) MoS₂ based catalyst (e-h) WS₂ based catalyst (i-l) Mo-W-S based catalyst; S2: BET surface area comparison for Pt supported catalyst on bulk MoS₂, WS₂, Mo-W-S; S3: XPS survey spectra of Pt/3D-MoS₂-MW, Pt/2D-WS₂-MW, Pt/2D-Mo-W-S-MW and Pt/3D-Mo-W-S-MW; S4: Yield of hydrogenation products as a function of time. See DOI: [URL – format <https://doi.org/DOI>]

Raw data for this article, including SEM and TEM images, EDS maps, XRF and XRD data are available at Zenodo under this DOI: <https://doi.org/10.5281/zenodo.17886350>.

Acknowledgements

This research was supported by the institutional support Dagmar Procházková Fund provided by University of Chemistry and Technology in Prague and by the Czech Science Foundation (GACR No. 23-08083M).

Notes and references

- L. Li, Z.-F. Jiao, J.-X. Zhao, D. Yao, X. Li and X.-Y. Guo, *J. Catal.*, 2023, **425**, 314–321.
- L. Zhong, X. Liao, H. Cui, J. Huang, H. Luo, Y. Lv and P. Liu, *ACS Catal.*, 2024, **14**, 15799–15810.
- X. Wang, X. Liang, P. Geng and Q. Li, *ACS Catal.*, 2020, **10**, 2395–2412.
- L. Yue, D. Sun, I. Mahmood Khan, X. Liu, Q. Jiang and W. Xia, *Food Chem.*, 2020, **309**, 125513.
- H. Liu, Q. Mei, S. Li, Y. Yang, Y. Wang, H. Liu, L. Zheng, P. An, J. Zhang and B. Han, *Chemical Communications*, 2018, **54**, 908–911.
- K. Nuithitikul and M. Winterbottom, in *Chemical Engineering Science*, 2004, vol. 59, pp. 5439–5447.
- S. Jiménez, J. A. López, M. A. Ciriano, C. Tejel, A. Martínez and R. A. Sánchez-Delgado, *Organometallics*, 2009, **28**, 3193–3202.
- S. Padmanaban, Y. Lee and S. Yoon, *Journal of Industrial and Engineering Chemistry*, 2021, **94**, 361–367.
- M. Zhang, Y. Sun, X. Zhou, K. Yang, L. Sun, C. Qi and M. Zhang, *Chemical Engineering Journal*, 2024, **479**, 147595.
- Q. Lu, H. Wang, J. Sun, X.-Z. Wei, Q. Zhang, X. Zhang, L. Chen, J. Liu, Y. Chen and L. Ma, *Microporous and Mesoporous Materials*, 2024, **367**, 112979.
- L. Wang, Y. Ma, H. Li, W. Luo and J. Liu, *J. Catal.*, 2024, **431**, 115391.
- A. J. Marchi, D. A. Gordo, A. F. Trasarti and C. R. Apesteguía, *Appl. Catal. A Gen.*, 2003, **249**, 53–67.
- F. Tian, M. Zhang, X. Zhang, X. Chen, J. Wang, Y. Zhang, C. Meng and C. Liang, *J. Mater. Sci.*, 2022, **57**, 3168–3182. [View Article Online https://doi.org/10.1039/D5CY01520K](https://doi.org/10.1039/D5CY01520K)
- X. Gao, Y. Ma, Y. Ruan, W. Zhang, S. Zhang, W. Xiong, D. Tian, S. Yang, P. Fan, Y. Yang and Y. Dai, *Molecular Catalysis*, 2024, **559**, 114096.
- H. Shi, Y. Xu, T. Su, X. Luo, X. Xie, Z. Qin and H. Ji, *Catal. Sci. Technol.*, 2024, **14**, 1181–1190.
- T. Yuan, D. Liu, Y. Pan, X. Pu, Y. Xia, J. Wang and W. Xiong, *Catal. Letters*, 2019, **149**, 851–859.
- X. Yuan, J. Zheng, Q. Zhang, S. Li, Y. Yang and J. Gong, *AIChE Journal*, 2014, **60**, 3300–3311.
- S. S. Mohire and G. D. Yadav, *Ind. Eng. Chem. Res.*, 2018, **57**, 9083–9093.
- S. Chen, L. Meng, B. Chen, W. Chen, X. Duan, X. Huang, B. Zhang, H. Fu and Y. Wan, *ACS Catal.*, 2017, **7**, 2074–2087.
- A. S. Nagpure, L. Gurralla, P. Gogoi and S. V. Chilukuri, *RSC Adv.*, 2016, **6**, 44333–44340.
- Z. Xu, C. Duong-Viet, Y. Liu, W. Baaziz, B. Li, L. Nguyen-Dinh, O. Ersen and C. Pham-Huu, *Appl. Catal. B*, 2019, **244**, 128–139.
- H. Ma, T. Yu, X. Pan and X. Bao, *Chinese Journal of Catalysis*, 2017, **38**, 1315–1321.
- Y. Zhang, S. Zhang, X. Pan, M. Bao, J. Huang and W. Shen, *Catal. Letters*, 2017, **147**, 102–109.
- C. Li, C. Ke, R. Han, G. Fan, L. Yang and F. Li, *Molecular Catalysis*, 2018, **455**, 78–87.
- Y. Zhang, C. Chen, W. Gong, J. Song, Y. Su, H. Zhang, G. Wang and H. Zhao, *RSC Adv.*, 2017, **7**, 21107–21113.
- Y. Xue, H. Xin, W. Xie, P. Wu and X. Li, *Chemical Communications*, 2019, **55**, 3363–3366.
- D. Hu, W. Fan, Z. Liu and L. Li, *ChemCatChem*, 2018, **10**, 779–788.
- Z. Tian, Q. Li, J. Hou, Y. Li and S. Ai, *Catal. Sci. Technol.*, 2016, **6**, 703–707.
- S. Wei, Y. Zhao, G. Fan, L. Yang and F. Li, *Chemical Engineering Journal*, 2017, **322**, 234–245.
- L. Wang, Y. Ma, H. Li, W. Luo and J. Liu, *J. Catal.*, 2024, **431**, 115391.
- K. N. Patil, P. Manikanta, P. M. Srinivasappa, A. H. Jadhav and B. M. Nagaraja, *J. Environ. Chem. Eng.*, 2023, **11**, 109168.
- Y. Qu, H. Pan and C. T. Kwok, *Sci. Rep.*, 2016, **6**, 34186.
- M. Pitínová, A. Krnáčková, A. Shafiq, I. Danylo, L. Koláčny and M. Veselý, *Catal. Today*, 2025, **460**, 115473.
- G. Wang, X.-L. Jiang, Y.-F. Jiang, Y.-G. Wang and J. Li, *ACS Catal.*, 2023, **13**, 8413–8422.
- H. Li, L. Wang, Y. Dai, Z. Pu, Z. Lao, Y. Chen, M. Wang, X. Zheng, J. Zhu, W. Zhang, R. Si, C. Ma and J. Zeng, *Nat. Nanotechnol.*, 2018, **13**, 411–417.
- F. Shi, W. Wu, J. Chen and Q. Xu, *Chemical Communications*, 2021, **57**, 7011–7014.
- I. Danylo, L. Koláčny, K. Kissíková, T. Hartman, M. Pitínová, J. Šturala, Z. Sofer and M. Veselý, *Nanoscale Adv.*, 2025, **7**, 2021–2031.
- Y.-J. Li, K. Dong, X.-K. Ma, J. Shi, J.-W. Fu, G.-W. Chu, H.-K. Zou and B.-C. Sun, *Sep. Purif. Technol.*, 2023, **315**, 123631.
- Z. Sofer, D. Sedmidubský, J. Luxa, D. Bouša, Š. Huber, P. Lazar, M. Veselý and M. Pumera, *Chemistry - A European Journal*, 2017, **23**, 10177–10186.
- M. Pitínová, I. Danylo, A. Shafiq, T. Hartman, M. Khover, B. Sevez, L. Koláčny and M. Veselý, *Catalysts*, 2025, **15**, 470.
- Y. Bai, N. Cherkasov, S. Huband, D. Walker, R. Walton and E. Rebrov, *Catalysts*, 2018, **8**, 58.



ARTICLE

Journal Name

- 42 K. ur Rehman, M. Gouda, U. Zaman, K. Tahir, S. U. Khan, S. Saeed, E. Khojah, A. El-Beltagy, A. A. Zaky, M. Naeem, M. I. Khan and N. S. Khattak, *Nanomaterials*, 2022, **12**, 1079.
- 43 Y. Qi, N. Wang, Q. Xu, H. Li, P. Zhou, X. Lu and G. Zhao, *Chemical Communications*, 2015, **51**, 6726–6729.
- 44 S. Arun, C. Arul, S. Mithin Kumar, U. Venkat Kiran and S. Mayavan, *ChemistrySelect*, 2020, **5**, 2469–2475.
- 45 X. Li, J. Pang, W. Luo, Y. Zhao, X. Pan and M. Zheng, *Catal. Letters*, 2021, **151**, 2734–2747.
- 46 A. Neog and R. Biswas, *Mater. Res. Bull.*, 2021, **144**, 111471.
- 47 Y. Q. Qin, Y. Q. Peng, W. F. Yang, Y. Wang, J. W. Cui and Y. Zhang, *IOP Conf. Ser. Mater. Sci. Eng.*, 2020, **770**, 012079.
- 48 G. Shen, Y. Yan, J. Tan and K. Hong, *J. Mater. Sci.*, 2022, **57**, 18819–18826.
- 49 G. Li, Y. Wang, J. Bi, X. Huang, Y. Mao, L. Luo and H. Hao, *Nanomaterials*, 2020, **10**, 278.
- 50 X. Zhang, J. Wang, H. Xu, H. Tan and X. Ye, *Nanomaterials*, 2019, **9**, 840.
- 51 M. Bandpey and D. P. J. Barz, *Nanoscale*, 2024, **16**, 15078–15093.
- 52 H. J. Sim, Z. Li, P. Xiao and H. Lu, *Molecules*, 2022, **27**, 7840.
- 53 Y. Sun, A. J. Darling, Y. Li, K. Fujisawa, C. F. Holder, H. Liu, M. J. Janik, M. Terrones and R. E. Schaak, *Chem. Sci.*, 2019, **10**, 10310–10317.

View Article Online
DOI: 10.1039/D5CY01520K



Data availability

The data supporting this article have been included as part of the Supplementary Information.

Supplementary information: S1: SEM images (a-d) MoS₂ based catalyst (e-h) WS₂ based catalyst (i-l) Mo-W-S based catalyst; S2: BET surface area comparison for Pt supported catalyst on bulk MoS₂, WS₂, Mo-W-S; S3: XPS survey spectra of Pt/3D-MoS₂-MW, Pt/2D-WS₂-MW, Pt/2D-Mo-W-S-MW and Pt/3D-Mo-W-S-MW; S4: Yield of hydrogenation products as a function of time. See DOI: [URL – format <https://doi.org/DOI>]

Raw data for this article, including SEM and TEM images, EDS maps, XRF and XRD data are available at Zenodo under this DOI: <https://doi.org/10.5281/zenodo.17886350>

